# Single-domain particles of manganese-for-iron substituted M-type barium hexaferrite: synthesis, crystal structure, and magnetic properties

Pavel E. Kazin[1], Anastasia E. Sleptsova[2], Alexander V. Vasiliev[1], Artem A. Eliseev[1], Robert E. Dinnebier[2], Sebastian Bette[2]

[1]Department of Chemistry, Lomonosov Moscow State University, Moscow, Russia
[2]Max Planck Institute for Solid State Research, Stuttgart, Germany

Corresponding author: Pavel E. Kazin, kazin@inorg.chem.msu.ru

ABSTRACT Single-phase barium hexaferrite powders with crystallite sizes in a single-domain region and with the general composition $BaFe_{12-x}Mn_xO_{19}$, where $x = 0, 2, 4, 6$, were synthesized applying a citric sol-gel auto-combustion technique with final annealing temperatures of $900 - 1200$ °C. The crystal structures were refined, and the magnetic properties were studied. The observed variations in atomic positions with the Mn-for-Fe substitution revealed presence of Mn in three oxidation state +2, +3, and +4, with a preference of $Mn^{2+}$ to the tetrahedral $4f_1$ site and $Mn^{4+}$ to the octahedral 2a and 12k sites. With the Mn-doping, the samples' magnetization decreased, while coercivity increased and reached 8.4 kOe for $x = 6$. The rise of the annealing temperature resulted in a slight growth of magnetization with a general tendency of the coercivity to decrease. A Curie temperature decreased with the Mn-doping remaining above room temperature for the maximal doping.

KEYWORDS magnetic materials, ferrites, crystal structure, magnetization, coercivity

## 1. Introduction

M-type hexaferrites are widely used to produce permanent magnets due to their excellent chemical and thermal stability and due to the low production costs, despite their moderate magnetic parameters such as magnetic energy and coercivity [1]. Besides that, there are very good prospectives for their application in ultra-high frequency devices functioning up to THz frequencies as well as in medium for high-density magnetic recording [2, 3]. Variation in the chemical composition of hexaferrite has proven to be an excellent instrument to adjust and optimize the material magnetic properties [4, 5]. This way, e.g., a giant coercivity and a sub-terahertz resonance have been achieved for an Al–Ca co-doped strontium hexaferrite [6, 7]. However, in many cases the results of the hexaferrite doping are hard to predict because of the complex crystal structure in which the dopant atoms may prefer different crystallographic sites. In particular, partial substitution of $Fe^{3+}$ by $Mn^{3+}$ in $MFe_{12}O_{19}$ (M = Ba, Sr) resulted not only in the non-uniform site occupancies but also in the variation of the dopant atom oxidation state [8–11]. Using neutron diffraction, it was shown that in $BaFe_{12-x}Mn_xO_{19}$, Mn preferred 2a, $4f_1$, 12k, and to a less extent $4f_2$ sites, whereas it was not found in 4e site [9]. The authors observed that the (Fe,Mn)–O distance in the tetrahedral $4f_1$ site tended to increase with the Mn-doping suggesting that $Fe^{3+}$ was replaced by $Mn^{2+}$ cations. Because of the limited accuracy of the crystal structure parameters determination, the authors did not observe distinct regularities in other (Fe,Mn)–O distances and offered only a tentative picture of the Mn ions distribution in different oxidation states in the crystal structure. The magnetic properties of such deep Mn-substituted hexaferrites were studied only for coarsely grained samples prepared by a standard ceramic technology. Whereas maximum coercivity values may be obtained for single-domain particles which possess sizes in nanometer and submicron regions. Possibly smaller particles, with the size in a nanometer scale, are especially attractive candidates for high-density magnetic recording [3]. For a small Mn-for-Fe substitution the study of submicron particles revealed certain enhancement in coercivity [12, 13]. Since an above-room-temperature ferrimagnetic order remains even in highly Fe-for-Mn substituted compounds, it looks useful to extend the study to deep Mn-doped hexaferrite samples representing ensembles of single-domain particles. In the present paper, we consider the synthesis of such $BaFe_{12-x}Mn_xO_{19}$ samples and investigate in detail their crystal structure and magnetic properties.

## 2. Experimental

### 2.1. Samples preparation

The preparation method was similar to that described in [14]. The starting compounds, chemically grade $BaCO_3$, $Fe(NO_3)_3 \cdot 9H_2O$, and $Mn(NO_3)_2 \cdot 4H_2O$, were taken in stoichiometric quantities corresponding to nominal compositions $BaFe_{12-x}Mn_xO_{19}$, where $x = 0, 2, 4, 6$. $BaCO_3$ was dissolved in an excess of 5 % nitric acid using magnetic stirring. Nitrates of iron and manganese were dissolved in the obtained solution. Solid citric acid was added to the solution in a stoichiometric quantity corresponding to 3 mol of acid per 1 mol of all metal cations, and the solution pH was adjusted to 7 by adding dropwise a 25 % ammonia solution. The resulting solution was slowly evaporated on a heated sand bath to a viscous state with consequent initiation of a self-propagating exothermal reaction. The obtained highly porous product was heated in a furnace in air for 2 hours to a certain annealing temperature $T_{an}$, dwelled for 2 hours at this temperature, and quenched in air. The annealing temperatures were 900, 1000, 1100, and 1200 $^\circ$C.

### 2.2. Samples characterization

High-precision X-ray powder diffraction (XRD) was conducted on a STOE STADI/P powder diffractometer in the Debay–Scherer geometry using $MoK_{\alpha1}$ radiation in the $2\theta$ range 2 – 110$^\circ$ with the $2\theta$ step of 0.015$^\circ$. The crystal structure was refined in the space group P6$_3$/mmc using the Jana 2006 computer program [15]. The reflection's profile parameters, unit cell parameters, positional and isotropic atomic displacement parameters were refined. Occupancies of Fe and Mn were fixed assuming a uniform distribution of the elements at 3d metal atom sites admitting full occupancies of the sites. Crystallite sizes (diameter $d$ and thickness $h$ of platelike particles in $ab$ plain and $c$ direction, respectively) were estimated by fitting a full XRD pattern profile taking into account broadening of the XRD reflections caused by instrumental parameters, crystallite sizes, and effects of crystal strain. Because of correlations between the crystallite size parameters and the strain parameters, only smaller size $h$ is reliably estimated with a large uncertainty though. To suppress the correlations, the strain parameters were assumed to be negligibly small and were set to zero. This allowed us to estimate both $d$ and $h$. The latter parameter after this procedure was reduced by 20 – 30 %. The parameters obtained this way may be regarded as lower boundary values for average crystallite sizes. These values have to approach real crystallite dimensions for crystals without defects. The parameters were estimated for the samples annealed at temperatures up to 1100 $^\circ$C. For $T_{an} = 1200$ $^\circ$C, the lines broadening due to a crystal size was too small to be reliably determined.

Measurements of magnetization were performed on an original Faraday Balance magnetometer at the room temperature in the field range $-17 - +17$ kOe. A powder sample was fixed with glue on a small piece of paper to prevent rotation of the particles in magnetic field.

Measurements of the Curie temperatures were carried out using a Perkin–Elmer Pyris Diamond TG/DTA with a permanent Fe–Nd–B magnet fixed outside the sample chamber. A transition from paramagnetic to ferrimagnetic state was registered by monitoring an effective weight of the sample on the sample cooling with a rate of 10 K·min$^{-1}$.

Scanning electron microscopy observations were performed on a Carl Zeiss Leo Supra VP50 electron microscope.

## 3. Results and discussion

### 3.1. Crystal structure features and morphology

As evidenced from the XRD analysis all the samples comprise pure hexaferrite phases with a hexagonal crystallographic symmetry. According to the scanning electron microscopy, samples annealed at 900 $^\circ$C consist of grains looking like thick plates with a typical diameter of 100 – 200 nm and thickness of 50 – 100 nm (Fig. A1, Appendix). With the increasing of the annealing temperature, the grains grow reaching a diameter of 300 – 400 nm and thickness of 100 – 200 nm for $T_{an} = 1100$ $^\circ$C. For $T_{an} = 1200$ $^\circ$C, a further and considerable increase in the grain size takes place. The crystallites become more anisotropic in shape and represent rounded plates with an average diameter of 0.7 micron in the undoped sample and 1 – 2 microns in the doped samples. The XRD peaks profile analysis provides values for the crystallites diameter and thickness (Table 1) corresponding well to the SEM results. This implies that the observed grains are single crystals. They have to be perfect enough since the line broadening connected to crystal defects and strains was considered as a negligible one in the XRD analysis. In general, undoped samples contain somewhat thicker platelike particles than Mn-doped ones. For the lowest annealing temperature, Mn-doped samples have slightly finer grains. With the $T_{an}$ increase, a stronger growth of grains takes place in Mn-doped samples, and the most pronounced effect is observed in the sample with the maximum Mn content.

The critical diameter $d_c$ for a $BaFe_{12}O_{19}$ grain to represent a single magnetic domain is of 0.8 micron [4]. The Mn-doping usually leads to reduction of saturation magnetization $M_s$ [8, 9], and $d_c$ is expected to grow with the doping since it is inversely proportional to $M_s^2$. Therefore, we regard that all the samples obtained represent ensembles of mostly monodomain grains. It especially concerns the samples annealed at lower temperatures.

The XRD patterns of all the samples are shown in Figs. A2–A17. The major results of the crystal structure refinement are collected in Table A1. Complete lists of atomic parameters are presented in Tables A2 and A3 for two limiting compositions, $BaFe_{12}O_{19}$ and $BaFe_6Mn_6O_{19}$, for the samples annealed at 1200 $^\circ$C. The dependencies of the crystal cell

TABLE 1. Crystallite diameter $d$ (nm) and thickness $h$ (nm) estimated from the full-profile XRD powder pattern analysis for $BaFe_{12-x}Mn_xO_{19}$. Standard deviation values are presented in parentheses.

| $x$ | $T_{an} = 900\ °C$ | | $T_{an} = 1000\ °C$ | | $T_{an} = 1100\ °C$ | |
|---|---|---|---|---|---|---|
| | $d$ | $h$ | $d$ | $h$ | $d$ | $h$ |
| 0 | 184(4) | 77(1) | 244(5) | 130(2) | 282(6) | 175(4) |
| 2 | 177(4) | 63(1) | 244(6) | 106(2) | 263(6) | 107(2) |
| 4 | 144(2) | 69(1) | 226(6) | 76(1) | 285(7) | 104(2) |
| 6 | 152(3) | 63(1) | 280(9) | 78(1) | 399(17) | 131(3) |

parameters on the Mn doping level and the annealing temperature are depicted in Fig. 1. The atomic radii of $Fe^{3+}$ and $Mn^{3+}$ are practically equal and amount to 0.645 Å for coordination number 6 [16]. One could expect a negligible influence of the Mn doping, but it is not the case. The cell parameters distinctly depend on $x$. There is also a detectable, but smaller variation of the cell parameters with the annealing temperature. On going from $x = 0$ to $x = 6$, almost independently from $T_{an}$, $a$ increases by 0.2 %, $c$ drops by 0.3 %, so that $c/a$ decreases by 0.5 %. As a result, cell volume $V$ grows only slightly, by 0.2 %. The data correspond well to those obtained earlier for coarsely grained hexaferrites with similar composition [8].
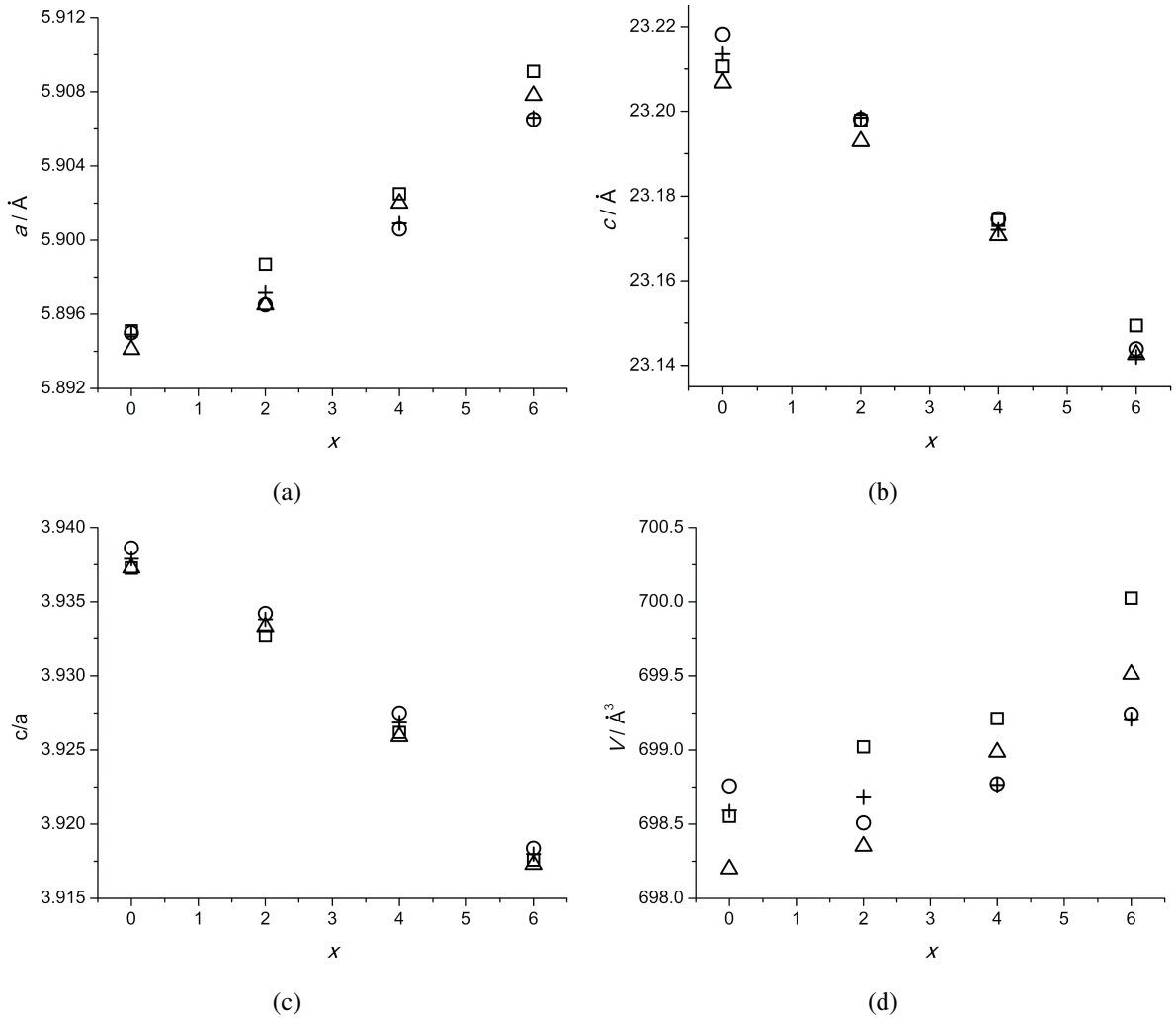


FIG. 1. The dependence of crystal cell parameters on Mn content $x$ in the $BaFe_{12-x}Mn_xO_{19}$ samples annealed at temperatures of 900 (circles), 1000 (crosses), 1100 (triangles), and 1200 °C (squares): (a) parameter $a$ (Å), (b) parameter $c$ (Å), (c) parameters' ratio $a/c$, (d) unit cell volume $V$ (Å$^3$).

Despite the observed small variation of the cell parameters and the volume, some of interatomic distances change much stronger with the doping. It should be noted that by the X-ray diffraction it is virtually impossible to distinguish Mn from Fe, therefore, we did not determine the distribution of Mn and Fe between the transition metal (M) sites. However, the changes in certain M–O distances may indicate that Mn substitute Fe at the corresponding sites acquiring an oxidation state different from +3.

The crystal structure of barium hexaferrite may be considered as a distorted close packing of oxygen atoms forming a five layers' set with a thickness of $c/2$. The set includes S-block with a spinel structure and R-block containing Ba atoms. 1st oxygen layer includes Ba atoms replacing oxygen atoms and in addition Fe2 atoms at a split 2b site (resulting in a half-filled 4e site, M2). Fe2 shifts from the center of trigonal bipyramid of oxygen atoms along $z$ and acquires tetrahedral coordination. Fe4 atoms ($4f_2$ site, M4) are found between 1st and 2nd as well as between 5th and 1st oxygen layers in an octahedral coordination. Fe5 atoms (12k site, M5) are found between 2nd and 3rd as well as between 4th and 5th oxygen layers in an octahedral coordination. Fe1 (2a site, M1) and Fe3 ($4f_1$ site, M3) atoms are found between 3rd and 4th oxygen layers in octahedral and tetrahedral coordination, respectively.

The changes in the interatomic distances are more pronounced for the samples, annealed at a maximum temperature of 1200 °C. Hence, we will analyze such distances for these samples. The dependence of average M–O distances on the Mn content is shown in Fig. 2. The strongest change takes place for the tetrahedral $4f_1$ site: $d$(M3–O) linearly grows from 1.887 to 1.980 Å (by ca. 5 %) on increasing $x$ from 0 to 6. For the M1 atom, found in the same layer, the corresponding distance, just in opposite, decreases from 2.014 to 1.977 Å (by ca. 2 %). A smaller decrease, from 2.032 to 2.008 Å (by ca. 1.2%), is observed for $d$(M5–O). Distances $d$(M2–O) and $d$(M4–O) are not appreciably affected by the Mn doping. Taking into account equal radii (R) of $Mn^{3+}$ and $Fe^{3+}$ and admitting that Mn cannot occupy the same site as $Mn^{2+}$ and $Mn^{4+}$ (due to very large difference in their sizes) we may estimate content of $Mn^{2+}$ and $Mn^{4+}$ for every site. For a tetrahedral coordination, R($Fe^{3+}$) = 0.49 Å and R($Mn^{2+}$) = 0.66 Å [15]. Then the change of $d$(M3-O) corresponds to 55(5) % of $Mn^{2+}$ at $4f_1$ site in $BaFe_6Mn_6O_{19}$. For an octahedral coordination, R($Fe^{3+}$) = 0.645 Å and R($Mn^{4+}$) = 0.53 Å [16]. That corresponds to 32(7) % of $Mn^{4+}$ at 2a site and 21(6) % of $Mn^{4+}$ at 12k site. Due to comparable quantities of $Mn^{4+}$ and $Mn^{2+}$ ions found in the structure the average oxidation state of Mn approaches +3.
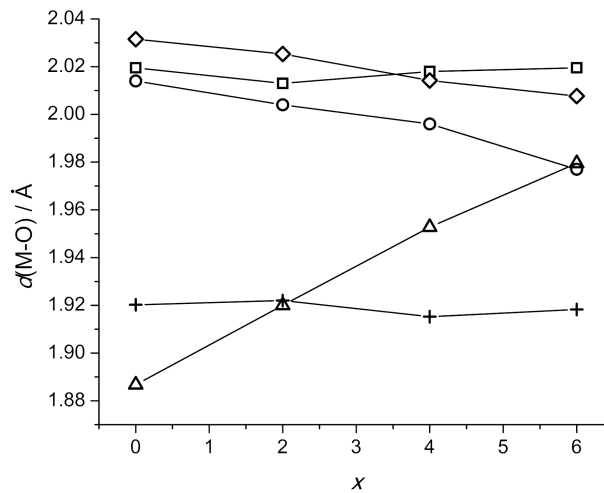


FIG. 2. The dependence of average distances $d$(M–O) between $3d$ metal atom M (Fe, Mn) and oxygen atoms of the coordination sphere on Mn content $x$ in the $BaFe_{12-x}Mn_xO_{19}$ samples annealed at 1200 °C: M1 (2a) – circles, M2 (4e) – crosses, M3 ($4f_1$) – triangles, M4 ($4f_2$) – squares, M5 (12k) – diamonds.

Occupancies of the M sites by Mn were estimated earlier for $BaFe_{12-x}Mn_xO_{19}$ ceramics using neutron powder diffraction [9]. For $BaFe_6Mn_6O_{19}$ they corresponded to 0.73, 0.73, 0.27, and 0.54 for M1, M3, M4, and M5 sites, respectively. No Mn was found at M2 site. We expect that a similar distribution of Mn ions takes place in our finely-grained samples. While the direct determination of Mn occupancies is not possible, the observed atomic displacement parameters $U_{eq}$ of M sites reflect such occupancies (see Tables A2 and A3). In $BaFe_{12}O_{19}$, $U_{eq}$ values for all 3d metal sites are close, while in $BaFe_6Mn_6O_{19}$, $U_{eq}$ correlates with the reported site occupancies, growing with the increase of the Mn occupancy. Combining the data [9] and our results we may suggest that (i) at $4f_1$ site, major part of Mn is in oxidation state +2, (ii) at 2a site, approximately half of Mn is in oxidation state +4, (iii) at 12k site, from one third to half of Mn is present as $Mn^{4+}$, and (iv) at $4f_2$ site, Mn is mostly in oxidation state +3. It is interesting that, while $d$(M2–O) does not vary with the Mn content (which is in accordance with the reported absence of Mn at 4e site [9]), the distances to apical oxygen (O1) and to those (O3) at the trigonal base of the distorted tetrahedron vary strongly. $d$(M2–O1) decreases from 2.138 to 2.072 Å and $d$(M2–O3) increases from 1.847 to 1.867 Å on going from $BaFe_{12}O_{19}$ to $BaFe_6Mn_6O_{19}$. Most

probably, the observed changes are determined by a local structure distortion due to Mn incorporation in other M sites. $Fe^{3+}$ at the M2 site provides the major magnetic anisotropy [17]. Our modelling of the $Fe^{3+}$ electronic structure using the CONDON program [18] shows that such lengthening of $d(Fe2–O3)$ reduces the axial magnetic anisotropy.

Apparently, strong variations in interatomic distances on the Mn doping compensate each other so that the change in the crystal cell parameters and volume becomes approximately one order of magnitude smaller. Such a compensation phenomenon is convenient to discuss considering variation in weighted average distances (along $z$ axis) between the oxygen atomic layers, which we denote as $h(n, m) = \Delta z/c$, where $n$ and $m$ are the numbers of oxygen layers (see Tables A2 and A3 for reference). Due to the crystal symmetry $h(5, 1) = h(1, 2)$ and $h(4, 5) = h(2, 3)$. In the undoped $BaFe_{12}O_{19}$ sample, $h(1, 2) = 0.10047$, $h(2, 3) = 0.09687$, $h(3, 4) = 0.10532$. In the maximally doped $BaFe_6Mn_6O_{19}$ sample, $h(1, 2) = 0.09993$, $h(2, 3) = 0.09499$, $h(3, 4) = 0.11016$. Thus, $h(3, 4)$ reveals an increase with the biggest absolute value, apparently, due to a large quantity of $Mn^{2+}$ at $4f_1$ site, which effect is not fully compensated by $Mn^{4+}$ at 2a site. $h(2, 3)$ decreases moderately and $h(1, 2)$ diminishes only slightly in consistence with the estimated $Mn^{4+}$ occupancies. The changes in the interlayer distances for 5 consecutive oxygen layers are listed as follows: $-0.5$, $-1.9$, $4.8$, $-1.9$, $-0.5$ %. This compensates the alteration of the crystal cell parameter $c$. Situated between the 3rd and 4th oxygen layers, the M3 ($4f_1$) coordination tetrahedron expands both, in the $c$ direction and in the $ab$ plain, while the M1 (2a) coordination octahedron, expanding in the $c$ direction, shrinks in the $ab$ plain. As a result, the cell parameter $a$ increases only slightly. The observed small multidirectional deformation of the hexaferrite crystal lattice was commonly attributed to the Jahn–Teller effect of $Mn^{3+}$ [8, 9]. In contrast to this, our study suggests that the stronger distortions affecting the net values of $a$ and $c$ are connected to simultaneous presence of non-Jahn–Teller $Mn^{2+}$ and $Mn^{4+}$ ions, rather than to the Jahn–Teller distortion of the $Mn^{3+}$ polyhedron.
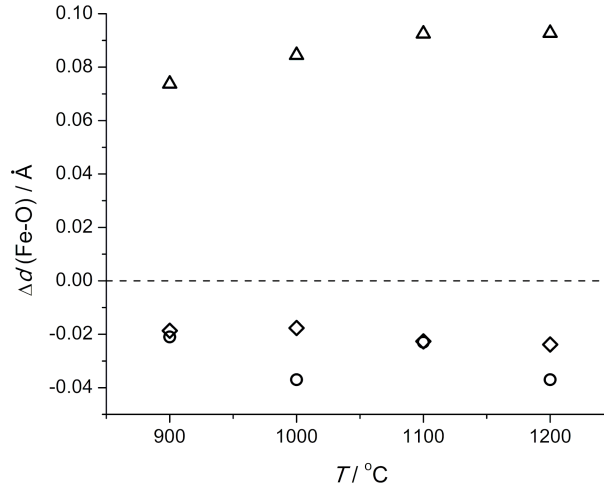


FIG. 3. The dependence of difference $\Delta d(M–O)$ between average distances $d(M–O)$ in $BaFe_6Mn_6O_{19}$ and $BaFe_{12}O_{19}$ on samples annealing temperature $T_{an}$: M1 (2a) – circles, M3 ($4f_1$) – triangles, M5 (12k) – diamonds.

Another interesting issue is possible dependence of $Mn^{4+}$ and $Mn^{2+}$ content on the sample annealing temperature and thus on the hexaferrite grain size. In Fig. 3, the differences $\Delta d(M–O)$ between average distances $d(M–O)$ in $BaFe_6Mn_6O_{19}$ and $BaFe_{12}O_{19}$ are shown for the samples annealed at different temperatures. In general, $\Delta d(M1–O)$, $\Delta d(M3–O)$, and $\Delta d(M5–O)$ values are non-zero for the whole annealing temperature range, designating presence of $Mn^{4+}$ and $Mn^{2+}$ in all the samples. Determined with a better accuracy, $\Delta d(M3–O)$ and $\Delta d(M5–O)$ tend to decrease with decreasing $T_{an}$ and drop by ca. 20 % on the $T_{an}$ changing from 1200 to 900 °C. This implies that the degree of the $Mn^{3+}$ disproportionation to $Mn^{2+}$ and $Mn^{4+}$ in the hexaferrite structure slightly decreases with lowering the sample annealing temperature and hence the grain size.

### 3.2. Magnetic properties

The dependence of the Curie temperature on the Mn content in the samples annealed at different temperatures is shown in Fig. 4. $T_C$ depends strongly on $x$ and very little on $T_{an}$. $T_C$ decreases with increasing the Mn content almost linearly, approximately 48 K per 1 Mn in the formula unit. Undoped samples show identical $T_C$ of 737 K for all the annealing temperatures. In Mn-doped samples $T_C$ decreases by 7 K with increasing $T_{an}$ from 900 to 1200 °C. This suggests that on the atomic scale, the changes in the undoped compound are negligible, whereas in the doped compounds, certain variations in the crystal structure may take place. Such variations may be connected to the disproportionation character of $Mn^{3+}$: the suggested above increase of the $Mn^{3+}$ disproportionation degree with the elevating annealing
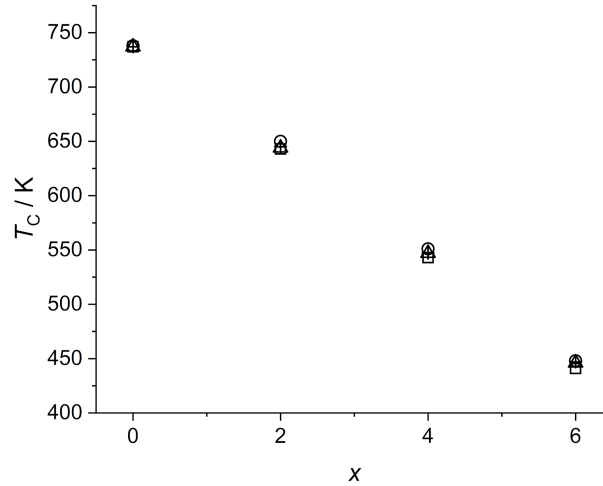
FIG. 4. The dependence of Curie temperature $T_C$ on Mn content $x$ in the $BaFe_{12-x}Mn_xO_{19}$ samples annealed at temperatures of 900 (circles), 1000 (crosses), 1100 (triangles), and 1200 °C (squares).

temperature may cause decrease of $T_C$. This is reasonable since the arising $Mn^{4+}$ ions in octahedral sites cannot efficiently take part in the antiferromagnetic exchange interaction because of the absence of electrons on the $e_g$ orbitals.

Magnetization and coercivity of the samples depend both, on the compound composition and the annealing temperature. To visualize better the latter dependence, in Fig. 5, magnetization and coercivity are displayed as a function of $T_{an}$. We analyze the magnetization of samples $M$ taken at the highest applied field of 17 kOe. As the magnetization curves approach to saturation, this magnetization value is assumed to be close to saturation magnetization. The magnetization considerably decreases with increasing the Mn content in the compound. This agrees well with the fact that $Mn^{3+}$ and $Mn^{4+}$, possessing lower magnetic moments than $Fe^{3+}$, occupy mostly sites of the major spin sublattice. In the undoped compound, $M$ tends to increase with increasing $T_{an}$. This may be related to healing the crystal structure defects. In the Mn-doped samples the effect is smaller, and in $BaFe_6Mn_6O_{19}$, the magnetization is nearly the same for all $T_{an}$. Possibly, the expected growth of magnetization is suppressed by the overlapped magnetization decrease owing to increase of the $Mn^{3+}$ disproportionation degree.
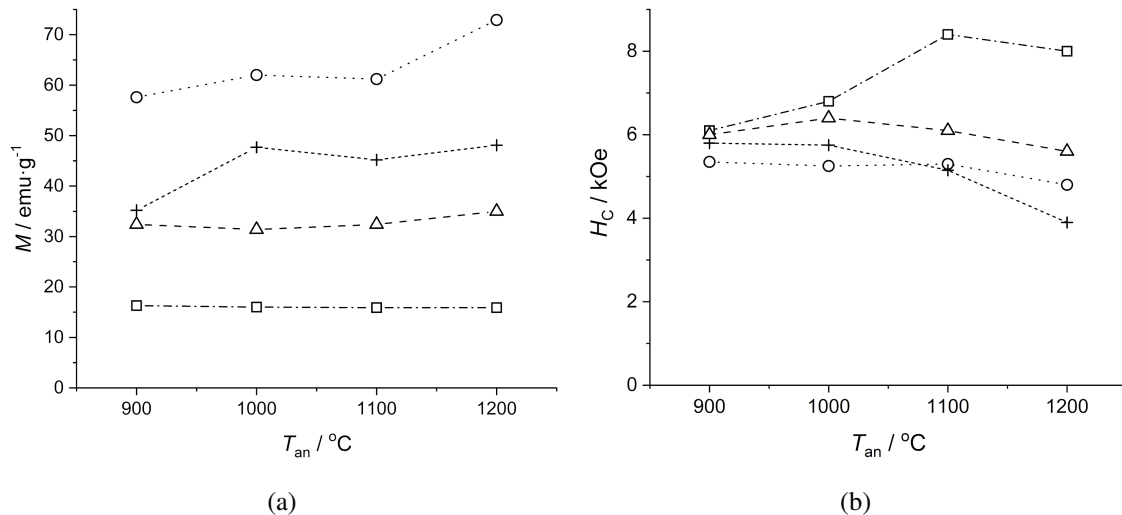


(a)

(b)

FIG. 5. The dependence of magnetization $M$ under a field of 17 kOe (a) and coercivity $H_c$ (b) on samples' annealing temperature $T_{an}$ in $BaFe_{12-x}Mn_xO_{19}$, where $x = 0$ (circles), 2 (crosses), 4 (triangles), 6 (squares).

Coercivities of the samples are high and, in most cases, exceed 5 kOe, which conforms with predominantly single-domain nature of the grains (crystallites). Coercivity of the undoped compound is nearly constant ($\sim 5.3$ kOe) for lower $T_{an}$, decreasing to 4.8 kOe only for $T_{an} = 1200$ °C. The latter may be related to growth of the grains so that the size of some of them exceeds a monodomain critical size. The compound with a low Mn content $x = 2$ shows somewhat increased coercivity of 5.8 kOe for $T_{an} = 900$ °C, which decreases to 3.9 kOe for $T_{an} = 1200$ °C. Probably, due to a larger grain size for $T_{an} = 1200$ °C and still substantial $M_s$, a higher fraction of grains is found in a multidomain

state. For the compounds with higher Mn content, the coercivity exhibits a maximum vs. $T_{an}$. The highest coercivity of 8.4 kOe is achieved for $BaFe_6Mn_6O_{19}$ annealed at 1100 °C. An analysis of interatomic distances sheds some light on the observed increase of $H_c$. The distance Fe2–O3 becomes shorter with increasing $T_{an}$, changing from 1.902 to 1.867 Å. And in accordance with the mentioned above theoretical calculations, such distance shortening should lead to a substantial raise of easy-axis magnetic anisotropy. The distance shortening may be in turn explained by rearrangement of other atoms because of increase of the $Mn^{3+}$ disproportionation degree. A small drop of coercivity for $T_{an} = 1200$ °C may be related to an enlargement of the crystallite size.

## 4.　Conclusions

Pure phase manganese for iron substituted barium hexaferrite samples $BaFe_{12-x}Mn_xO_{19}$ ($x = 0, 2, 4, 6$) were prepared by a sol-gel citrate method in the form of powders with crystallite sizes from tens of nanometers to about a micron, which ensured single domain nature of the compound grains. The variation in the grain size was achieved by the precursor annealing at temperatures 900 – 1200 °C. Detailed analysis of the crystal structure using powder X-ray diffraction data reveals small variations in the crystal cell parameters with the Mn substitution and the sample annealing temperature, and along with this, demonstrates an order of magnitude larger changes in interatomic distances. It is shown that $Mn^{3+}$ replacing $Fe^{3+}$ partially disproportionates to larger $Mn^{2+}$ ions occupying tetrahedral $4f_1$ sites and smaller $Mn^{4+}$ ions, occupying 2a and to a less extent 12k sites. The degree of disproportionation slightly grows with increasing the annealing temperature. The Curie temperature decreases almost linearly with $x$ from 737 to 448 K and, for Mn doped samples, drops other several degrees with increasing the annealing temperature in accordance with the change in the relative content of $Mn^{2+}$ and $Mn^{4+}$. The magnetization decreases with $x$, while coercivity tends to increase, reaching 8.4 kOe for the sample with $x = 6$ annealed at 1100 °C. To our knowledge, the obtained maximum value of coercivity is one of the highest among Mn doped hexaferrites conceding only to a coercivity of 9.7 kOe registered in a submicron-grained $SrFe_{12-x}Mn_xO_{19}$ prepared by a mechano-chemical route [19].

## Appendix

TABLE A1. Crystal cell parameters $a$ and $c$, $R$-factors, and average M–O distances $d$ (M = Fe, Mn) in $BaFe_{12-x}Mn_xO_{19}$, where $x = 0, 2, 4, 6$ (samples 1, 2 ,3, 4, respectively), annealed at 900, 1000, 1100, 1200 °C (samples' second symbol **a**, **b**, **c**, **d**, respectively). Values of $a$, $c$, and $d$ are in Å.
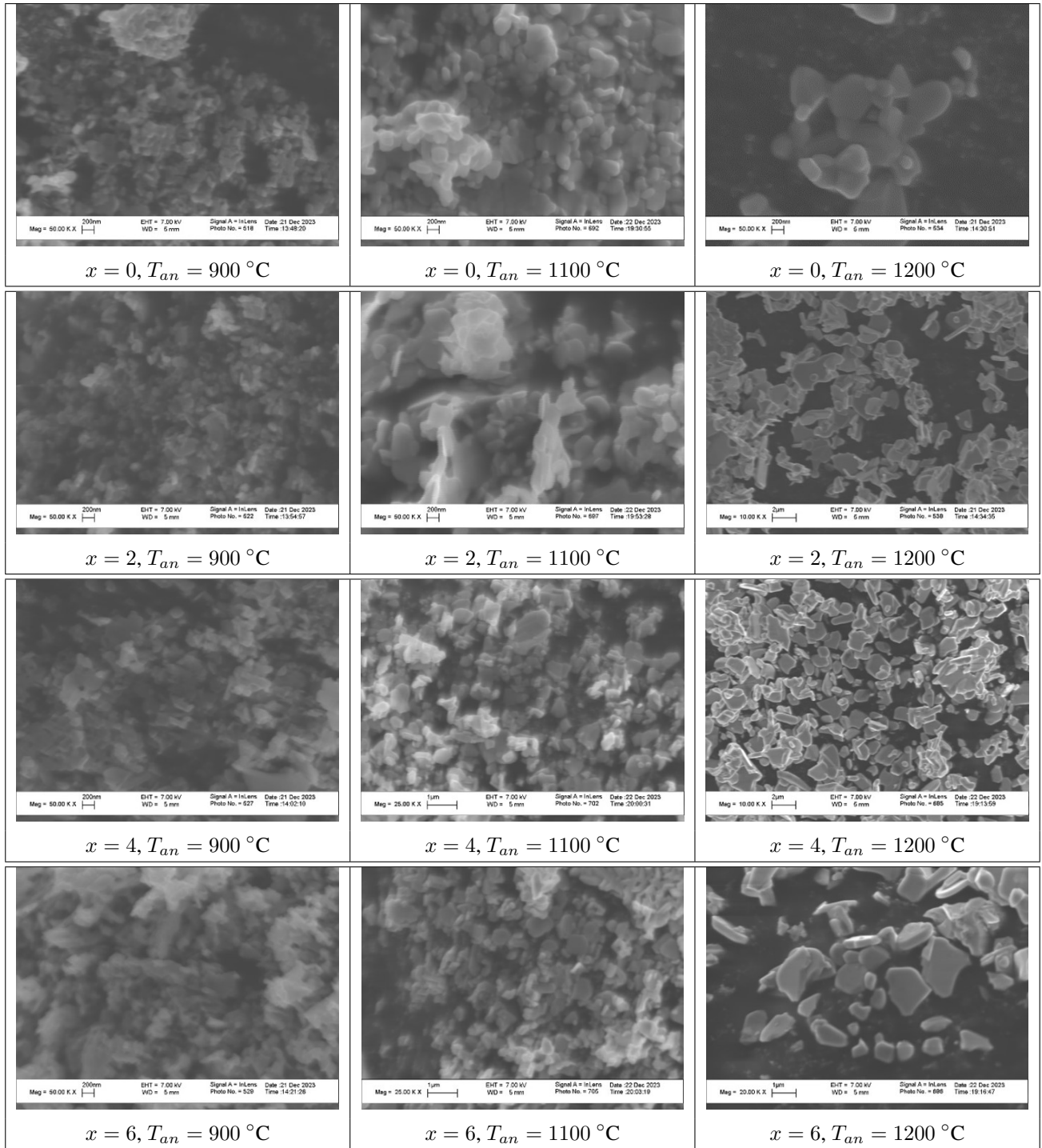
| Sample | $a$ (Å) | $c$ (Å) | $R_{wp}, R_{all}$ | $d$(M1-O) | $d$(M2-O) | $d$(M3-O) | $d$(M4-O) | $d$(M5-O) |
|--------|---------|---------|-------------------|-----------|-----------|-----------|-----------|-----------|
| **1a** | 5.8950(1) | 23.2182(3) | 0.031, 0.019 | 2.013(5) | 1.914(9) | 1.887(6) | 2.023(6) | 2.032(4) |
| **1b** | 5.8949(1) | 23.2135(2) | 0.029, 0.019 | 2.020(5) | 1.916(7) | 1.883(5) | 2.020(5) | 2.032(3) |
| **1c** | 5.8941(1) | 23.2067(2) | 0.036, 0.015 | 2.008(4) | 1.920(6) | 1.888(4) | 2.020(4) | 2.031(3) |
| **1d** | 5.8951(1) | 23.2106(2) | 0.038, 0.017 | 2.014(4) | 1.920(6) | 1.887(4) | 2.020(4) | 2.032(3) |
| **2a** | 5.8965(1) | 23.1981(3) | 0.031, 0.016 | 2.016(5) | 1.921(8) | 1.913(6) | 2.016(6) | 2.024(3) |
| **2b** | 5.8972(1) | 23.1985(3) | 0.028, 0.023 | 2.008(5) | 1.909(9) | 1.914(6) | 2.025(6) | 2.024(4) |
| **2c** | 5.8965(1) | 23.1929(2) | 0.035, 0.015 | 2.003(4) | 1.922(6) | 1.914(4) | 2.015(4) | 2.027(3) |
| **2d** | 5.8987(1) | 23.1978(2) | 0.039, 0.016 | 2.004(4) | 1.922(6) | 1.920(4) | 2.013(4) | 2.025(3) |
| **3a** | 5.9006(1) | 23.1746(3) | 0.028, 0.016 | 2.010(5) | 1.928(7) | 1.936(5) | 2.014(5) | 2.018(4) |
| **3b** | 5.9009(1) | 23.1720(3) | 0.028, 0.022 | 2.011(5) | 1.941(8) | 1.939(6) | 2.009(6) | 2.016(4) |
| **3c** | 5.9020(1) | 23.1707(2) | 0.030, 0.018 | 2.002(5) | 1.919(7) | 1.945(5) | 2.015(5) | 2.019(3) |
| **3d** | 5.9025(1) | 23.1743(2) | 0.042, 0.016 | 1.996(4) | 1.915(6) | 1.953(4) | 2.018(4) | 2.014(3) |
| **4a** | 5.9065(1) | 23.1439(3) | 0.027, 0.017 | 1.992(5) | 1.950(7) | 1.961(5) | 2.003(6) | 2.014(4) |
| **4b** | 5.9066(1) | 23.1420(3) | 0.028, 0.021 | 1.983(5) | 1.935(8) | 1.967(6) | 2.007(6) | 2.015(4) |
| **4c** | 5.9078(1) | 23.1426(3) | 0.029, 0.028 | 1.985(5) | 1.921(8) | 1.981(6) | 2.016(6) | 2.009(4) |
| **4d** | 5.9091(1) | 23.1494(2) | 0.042, 0.023 | 1.977(4) | 1.918(6) | 1.980(4) | 2.020(4) | 2.008(3) |

TABLE A2. Atomic parameters in the crystal structure of $BaFe_{12}O_{19}$ annealed at 1200 °C

| Atom | Occupancy | $x/a$ | $y/a$ | $z/c$ | $U_{iso}$ (Å$^2$) |
|------|-----------|-------|-------|-------|-------------------|
| Ba   | 1         | 2/3   | 1/3   | 1/4   | 0.0065(2)         |
| Fe1  | 1         | 0     | 0     | 0     | 0.0048(4)         |
| Fe2  | 0.5       | 0     | 0     | 0.25869(14) | 0.0039(6)   |
| Fe3  | 1         | 1/3   | 2/3   | 0.02733(6)  | 0.0045(3)   |
| Fe4  | 1         | 1/3   | 2/3   | 0.19032(5)  | 0.0047(3)   |
| Fe5  | 1         | 0.16853(9) | 0.33706(19) | 0.89168(3) | 0.0048(2) |
| O1   | 1         | 0     | 0     | 0.1492(2)   | 0.0063(4)   |
| O2   | 1         | 2/3   | 1/3   | 0.0540(2)   | 0.0063(4)   |
| O3   | 1         | 0.1799(5) | 0.3597(11) | 1/4    | 0.0063(4)   |
| O4   | 1         | 0.1575(4) | 0.3150(8)  | 0.05221(12) | 0.0063(4) |
| O5   | 1         | 0.5002(4) | 0.0003(8)  | 0.14964(13) | 0.0063(4) |

TABLE A3. Atomic parameters in the crystal structure of $BaFe_6Mn_6O_{19}$ annealed at 1200 °C

| Atom | Occupancy | $x/a$ | $y/a$ | $z/c$ | $U_{iso}$ (Å$^2$) |
|------|-----------|-------|-------|-------|-------------------|
| Ba   | 1         | 2/3   | 1/3   | 1/4   | 0.0093(2)         |
| M1   | 1         | 0     | 0     | 0     | 0.0095(5)         |
| M2   | 0.5       | 0     | 0     | 0.25908(14) | 0.0022(7)   |
| M3   | 1         | 1/3   | 2/3   | 0.02768(7)  | 0.0103(3)   |
| M4   | 1         | 1/3   | 2/3   | 0.19062(6)  | 0.0069(3)   |
| M5   | 1         | 0.16737(11) | 0.3347(2) | 0.89196(3) | 0.0082(2) |
| O1   | 1         | 0     | 0     | 0.1514(3)   | 0.0154(5)   |
| O2   | 1         | 2/3   | 1/3   | 0.0587(2)   | 0.0154(5)   |
| O3   | 1         | 0.1813(6) | 0.3626(12) | 1/4    | 0.0154(5)   |
| O4   | 1         | 0.1499(4) | 0.2998(8)  | 0.05387(14) | 0.0154(5) |
| O5   | 1         | 0.5012(4) | 0.0023(9)  | 0.14962(16) | 0.0154(5) |

*P. E. Kazin, A. E. Sleptsova, A. V. Vasiliev, A. A. Eliseev, R. E. Dinnebier, S. Bette*

| | | |
|---|---|---|
| $x = 0, T_{an} = 900\ °$C | $x = 0, T_{an} = 1100\ °$C | $x = 0, T_{an} = 1200\ °$C |
| $x = 2, T_{an} = 900\ °$C | $x = 2, T_{an} = 1100\ °$C | $x = 2, T_{an} = 1200\ °$C |
| $x = 4, T_{an} = 900\ °$C | $x = 4, T_{an} = 1100\ °$C | $x = 4, T_{an} = 1200\ °$C |
| $x = 6, T_{an} = 900\ °$C | $x = 6, T_{an} = 1100\ °$C | $x = 6, T_{an} = 1200\ °$C |

FIG. A1. Scanning electron microscopy images of $BaFe_{12-x}Mn_xO_{19}$ samples annealed at $T_{an}$
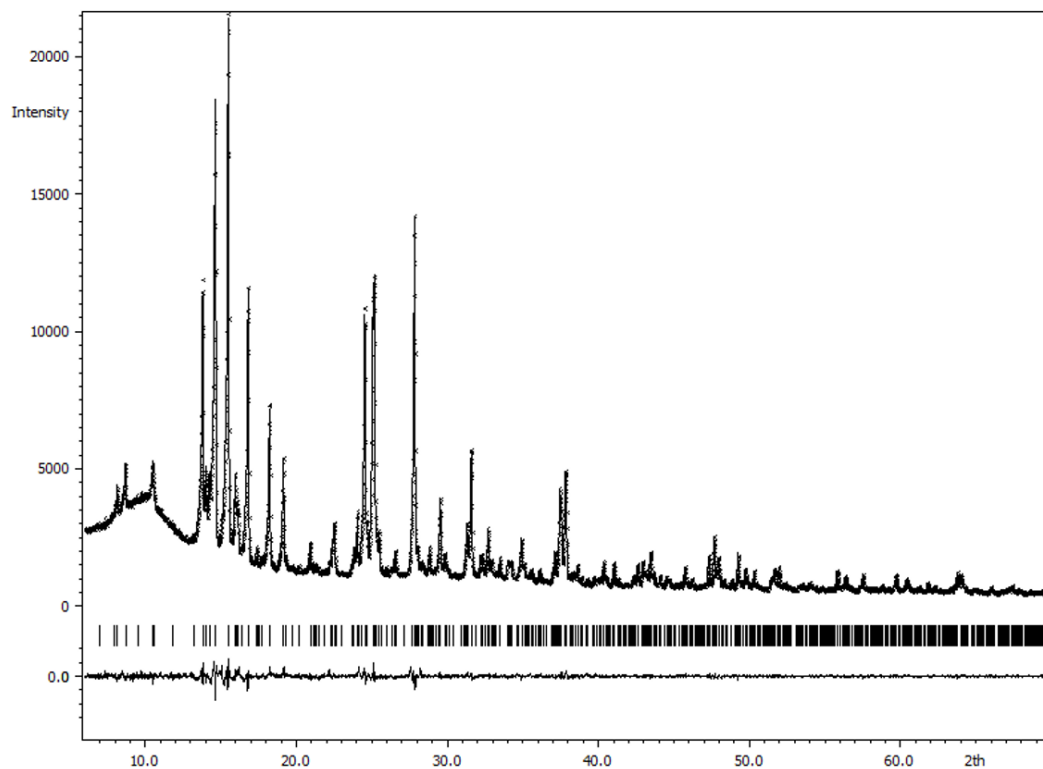
FIG. A2. Observed (crosses), calculated (line), and difference (line underneath) XRD patterns of $BaFe_{12-x}Mn_xO_{19}$, $x = 0$, $T_{an} = 900\,^{\circ}C$
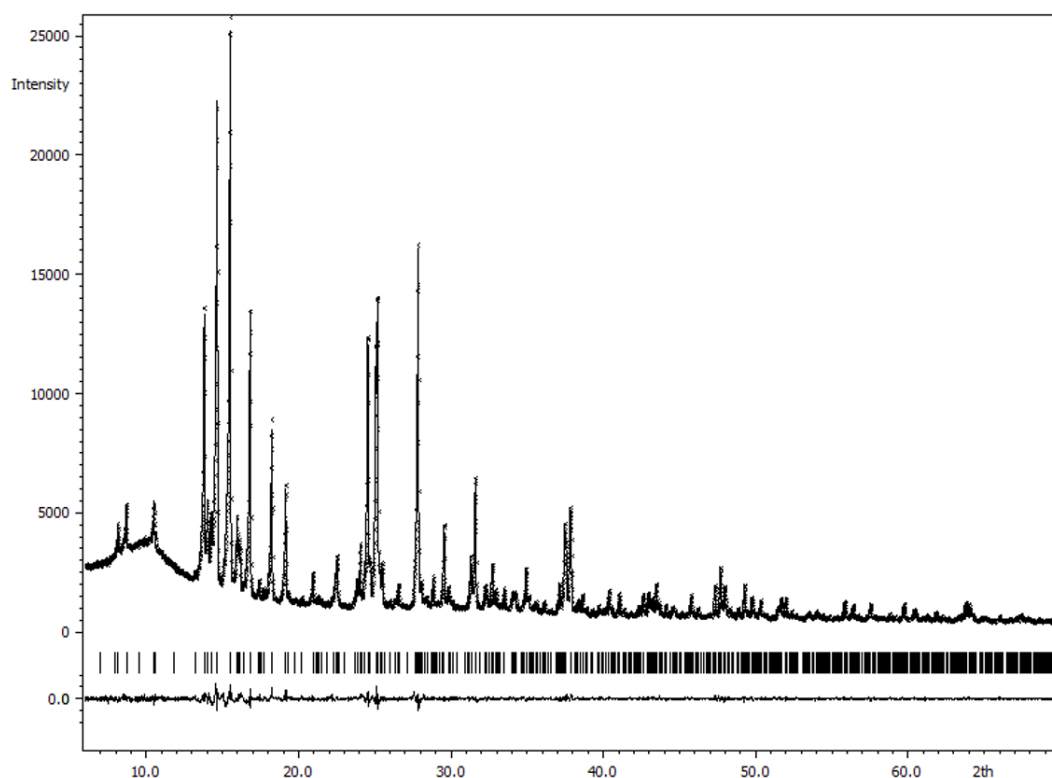


FIG. A3. Observed (crosses), calculated (line), and difference (line underneath) XRD patterns of $BaFe_{12-x}Mn_xO_{19}$, $x = 0$, $T_{an} = 1000\,^{\circ}C$
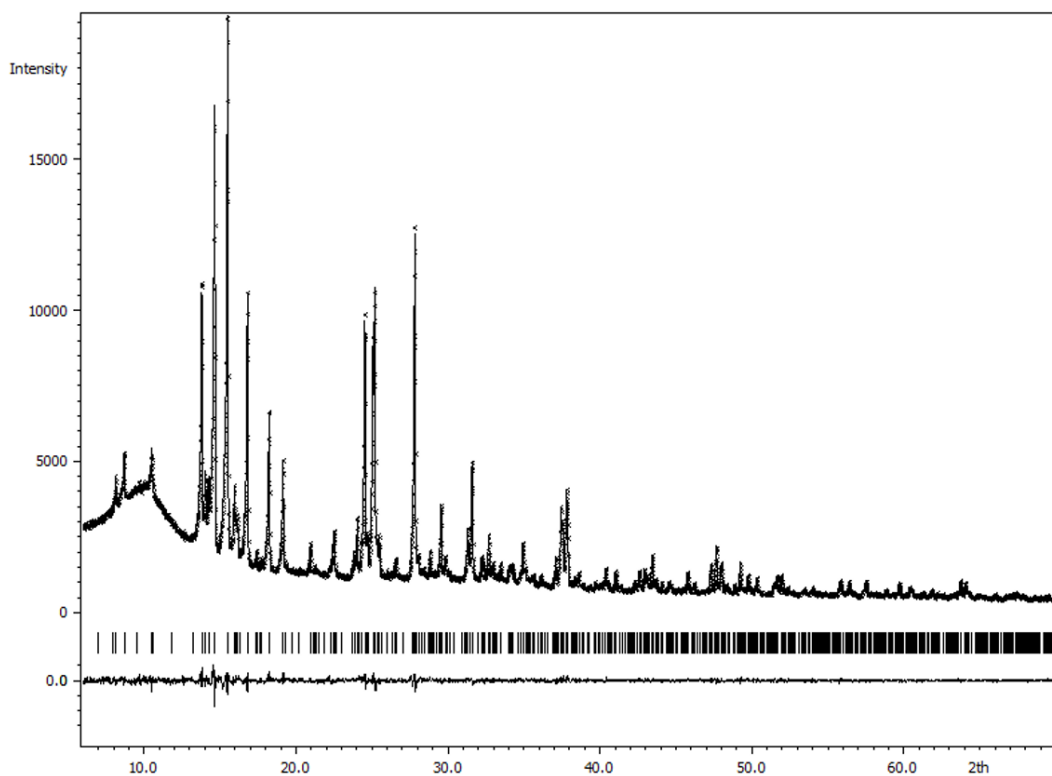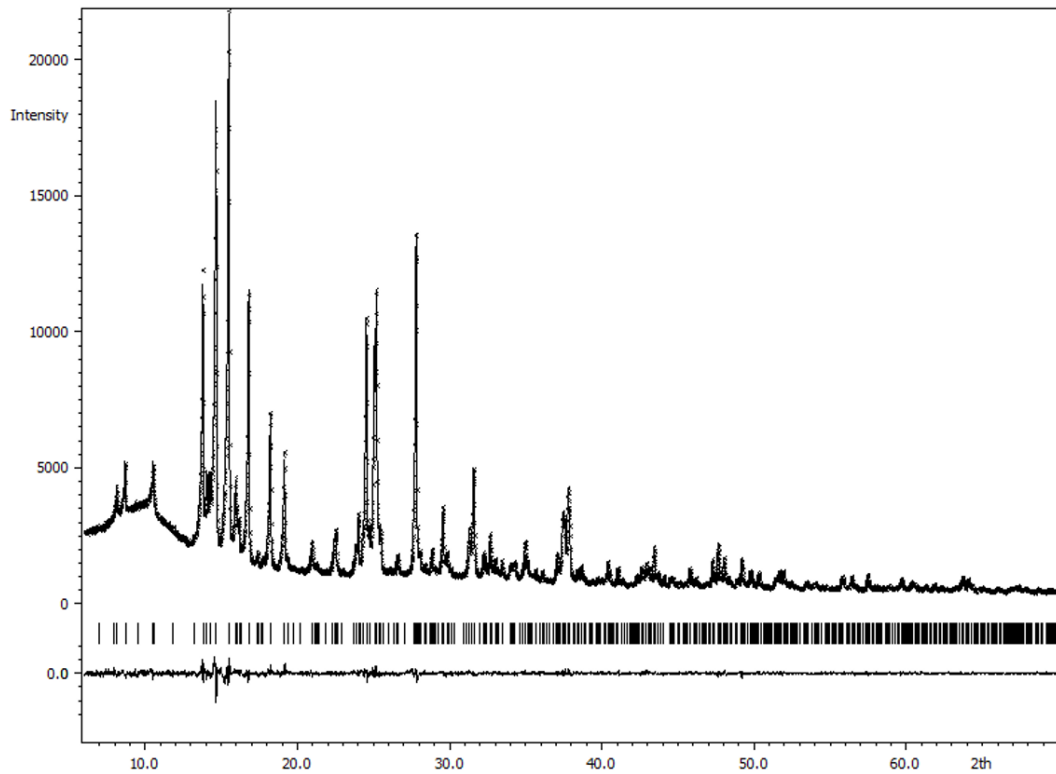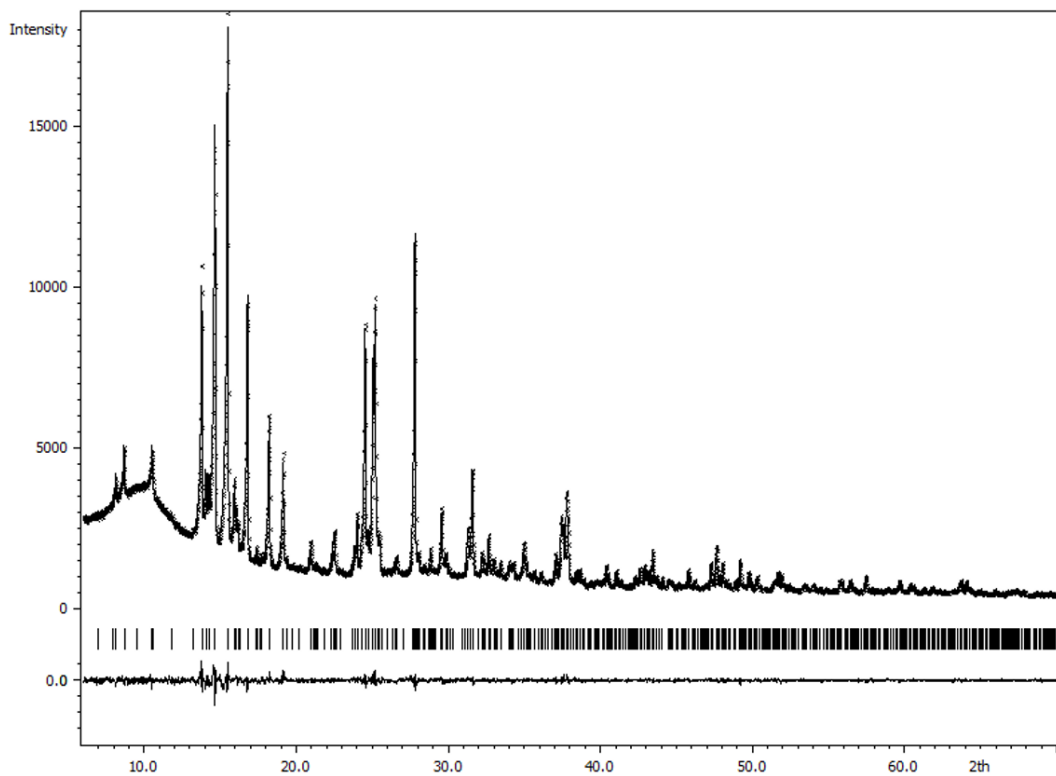
FIG. A4. Observed (crosses), calculated (line), and difference (line underneath) XRD patterns of $BaFe_{12-x}Mn_xO_{19}$, $x = 0$, $T_{an} = 1100$ °C
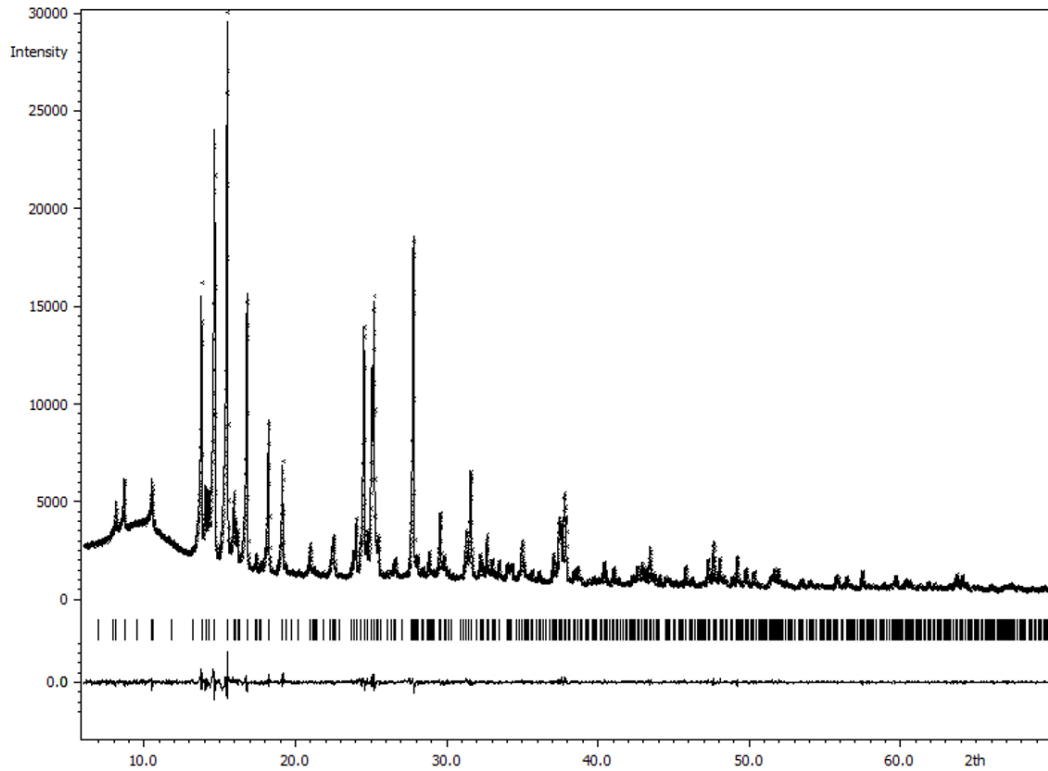


FIG. A5. Observed (crosses), calculated (line), and difference (line underneath) XRD patterns of $BaFe_{12-x}Mn_xO_{19}$, $x = 0$, $T_{an} = 1200$ °C
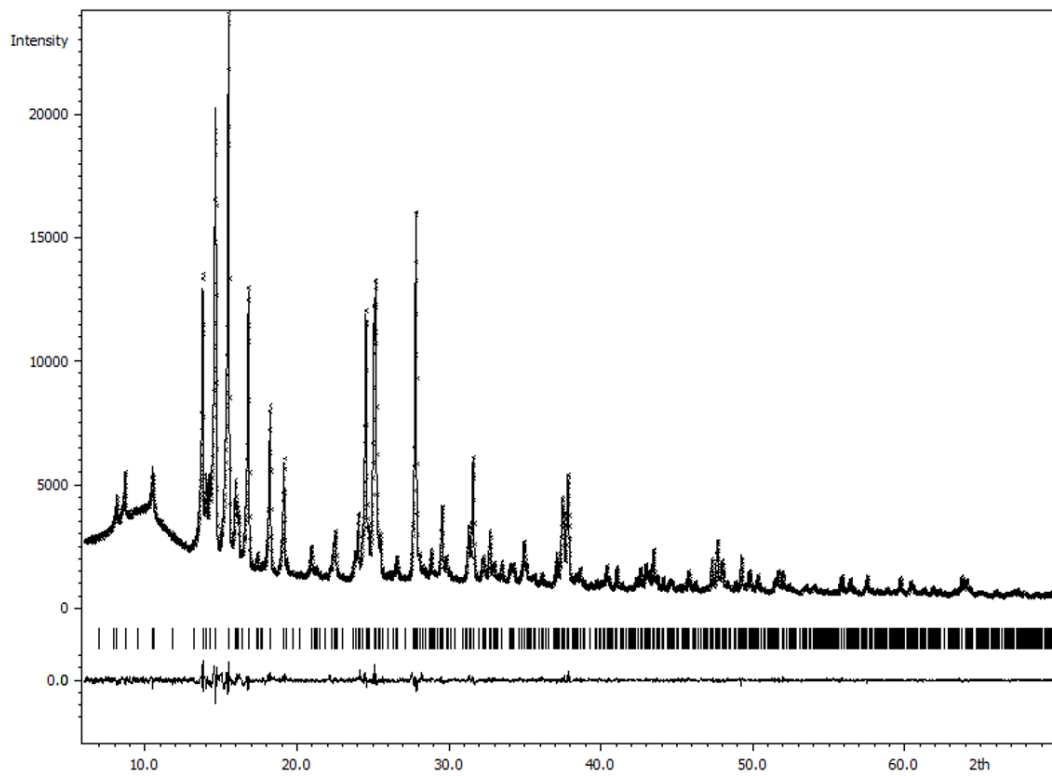
FIG. A6. Observed (crosses), calculated (line), and difference (line underneath) XRD patterns of $BaFe_{12-x}Mn_xO_{19}$, $x = 2$, $T_{an} = 900\,^{\circ}C$



FIG. A7. Observed (crosses), calculated (line), and difference (line underneath) XRD patterns of $BaFe_{12-x}Mn_xO_{19}$, $x = 2$, $T_{an} = 1000\,^{\circ}C$
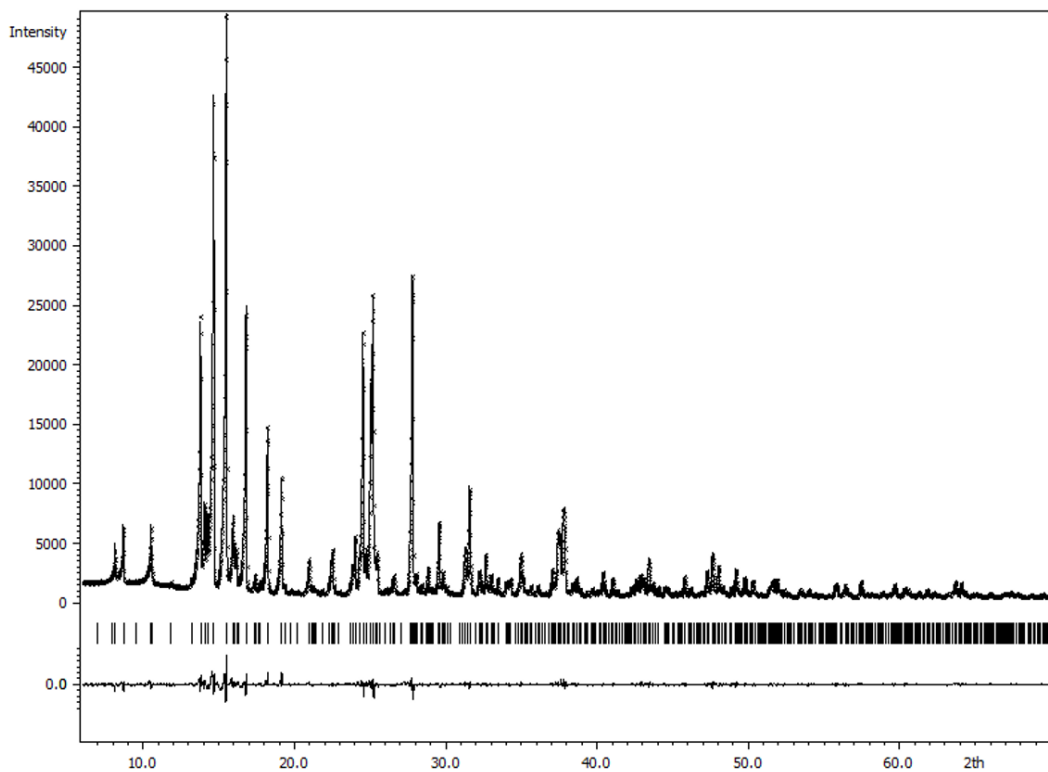
FIG. A8. Observed (crosses), calculated (line), and difference (line underneath) XRD patterns of $BaFe_{12-x}Mn_xO_{19}$, $x = 2$, $T_{an} = 1100\,^{\circ}C$



FIG. A9. Observed (crosses), calculated (line), and difference (line underneath) XRD patterns of $BaFe_{12-x}Mn_xO_{19}$, $x = 2$, $T_{an} = 1200\,^{\circ}C$

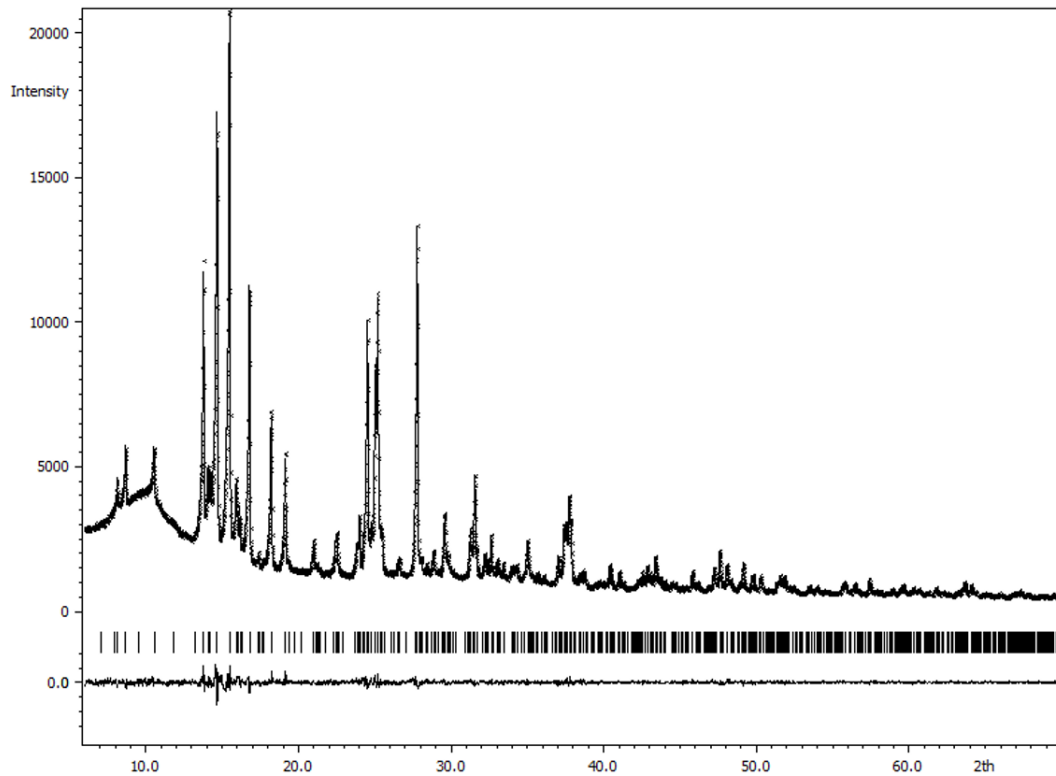FIG. A10. Observed (crosses), calculated (line), and difference (line underneath) XRD patterns of $BaFe_{12-x}Mn_xO_{19}$, $x = 4$, $T_{an} = 900\,°C$



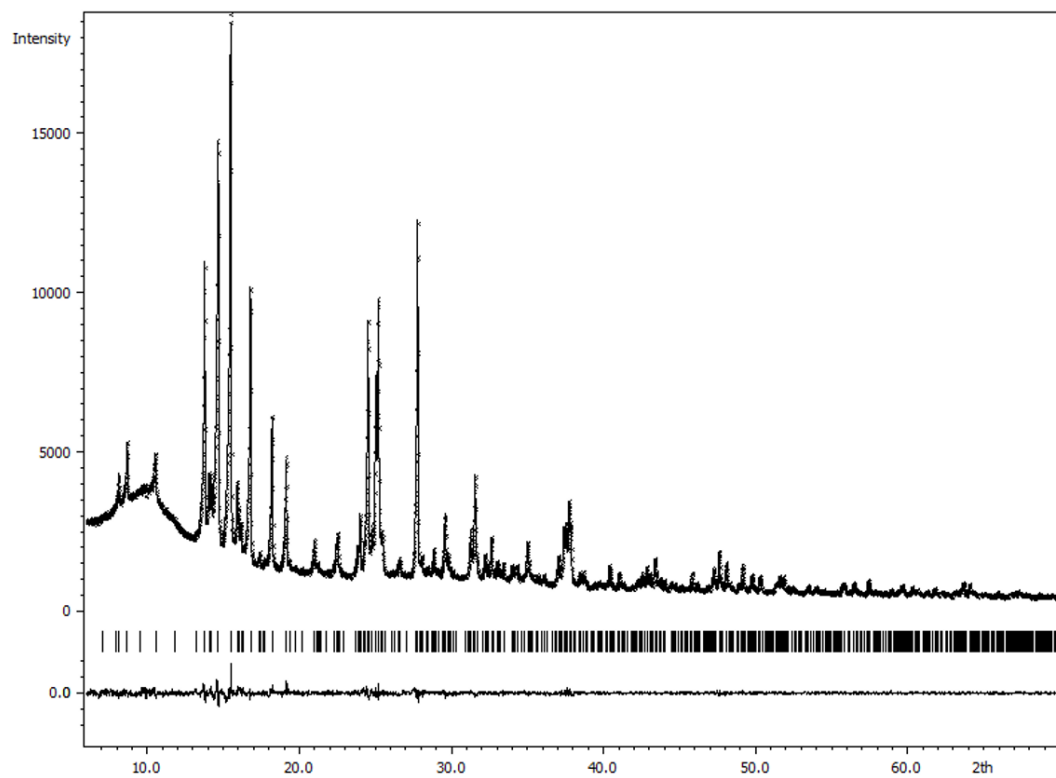FIG. A11. Observed (crosses), calculated (line), and difference (line underneath) XRD patterns of $BaFe_{12-x}Mn_xO_{19}$, $x = 4$, $T_{an} = 1000\,°C$

FIG. A12. Observed (crosses), calculated (line), and difference (line underneath) XRD patterns of $BaFe_{12-x}Mn_xO_{19}$, $x = 4$, $T_{an} = 1100\,^\circ C$



FIG. A13. Observed (crosses), calculated (line), and difference (line underneath) XRD patterns of $BaFe_{12-x}Mn_xO_{19}$, $x = 4$, $T_{an} = 1200\,^\circ C$

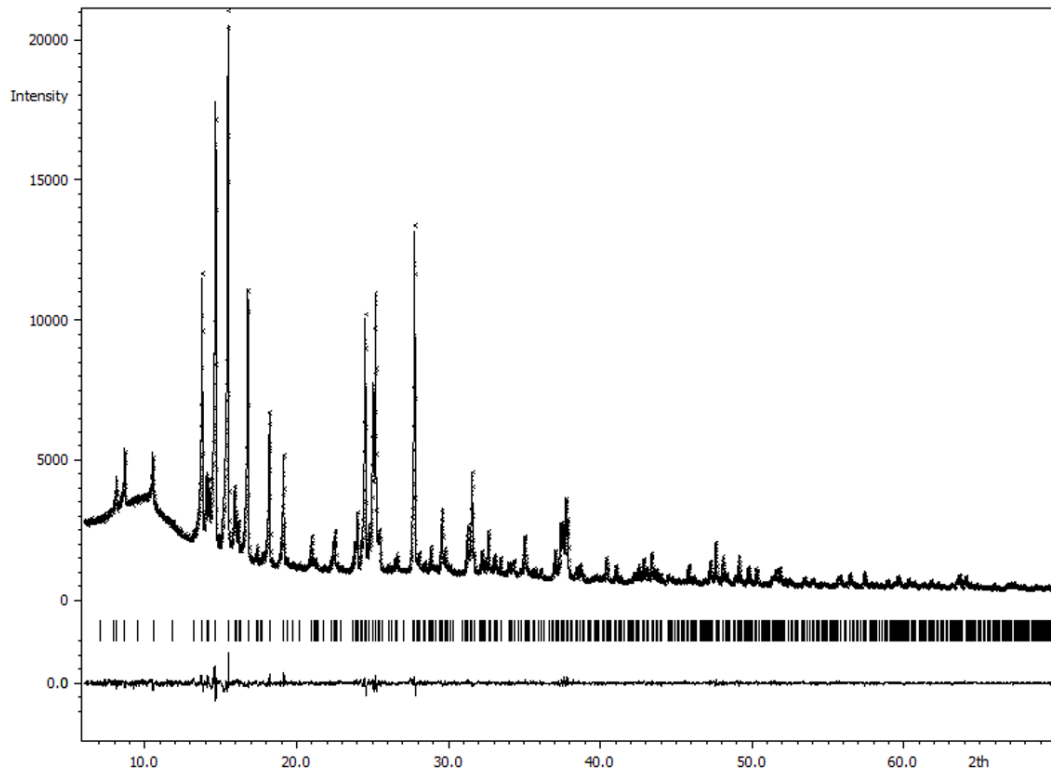FIG. A14. Observed (crosses), calculated (line), and difference (line underneath) XRD patterns of $BaFe_{12-x}Mn_xO_{19}$, $x = 6$, $T_{an} = 900\,^{\circ}C$



FIG. A15. Observed (crosses), calculated (line), and difference (line underneath) XRD patterns of $BaFe_{12-x}Mn_xO_{19}$, $x = 6$, $T_{an} = 1000\,^{\circ}C$

FIG. A16. Observed (crosses), calculated (line), and difference (line underneath) XRD patterns of $BaFe_{12-x}Mn_xO_{19}$, $x = 6$, $T_{an} = 1100\ ^\circ C$
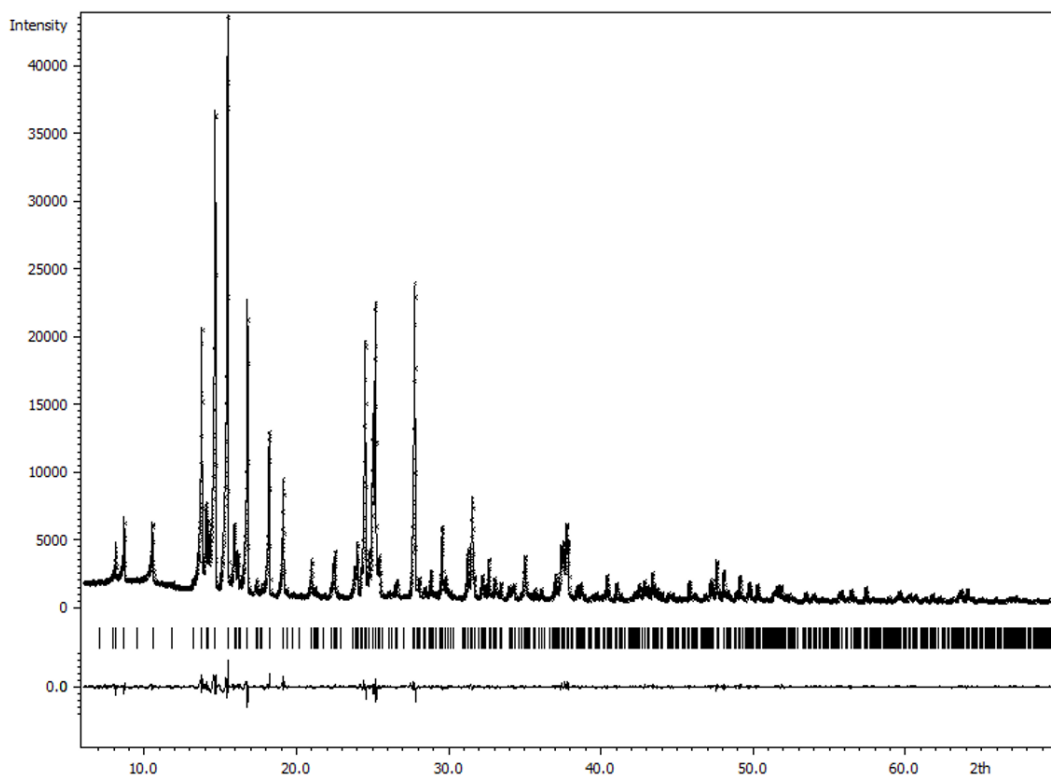


FIG. A17. Observed (crosses), calculated (line), and difference (line underneath) XRD patterns of $BaFe_{12-x}Mn_xO_{19}$, $x = 6$, $T_{an} = 1200\ ^\circ C$

## References

[1] Buschow K.H.J., de Boer F.R. *Physics of Magnetism and Magnetic Materials*, Kluwer Academic/Plenum Publishers, New York, 2003, 182 p.

[2] Harris V.G., Geiler A., Chen Y., Yoon S. D., Wu M., Yang A., Chen Z., He P., Parimi P. V., Zuo X., Patton C.E., Abe M., Acher O., Vittoria C. Recent advances in processing and applications of microwave ferrites. *J. Magn. Magn. Mater.*, 2009, **321**, P. 2035–2047.

[3] Shimizu O., Oyanagi M., Morooka A., Mori M., Kurihashi Y., Tada T., Suzuki H., Harasawa T. Development of advanced barium ferrite tape media. *J. Magn. Magn. Mater.*, 2016, **400**, P. 365–369.

[4] Pullar R.C. Hexagonal ferrites: A review of the synthesis, properties and applications of hexaferrite ceramics. *Prog. Mater. Sci.*, 2012, **57**, P. 1191–1334.

[5] Banihashemi V., Ghazi M.E., Izadifard M., Dinnebier R.E. A study of Ca-doped hexaferrite $Sr_{1-x}Ca_xFe_{12}O_{19}$ ($x = 0.0$, 0.05, 0.1, 0.15, and 0.2) synthesized by sol-gel combustion method. *Phys. Scr.*, 2020, **95**, 095807.

[6] Trusov L.A., Gorbachev E.A., Lebedev V.A., Sleptsova A.E., Roslyakov I.V., Kozlyakova E.S., Vasiliev A.V., Dinnebier R.E., Jansen M., Kazin P.E. Ca-Al double-substituted strontium hexaferrites with giant coercivity. *Chem. Commun.*, 2018, **54**, P. 479–482.

[7] Gorbachev E.A., Trusov L.A., Sleptsova A.E., Kozlyakova E.S., Alyabyeva L.N., Yegiyan S.R., Prokhorov A.S., Lebedev V.A., Roslyakov I.V., Vasiliev A.V., Kazin P.E. Hexaferrite materials displaying ultra-high coercivity and sub-terahertz ferromagnetic resonance frequencies. *Mater. Today*, 2020, **32**, P. 13–18.

[8] Obradors X., Collomb A., Pernet M., Jourbert J.C. Structural and magnetic properties of $BaFe_{12-x}Mn_xO_{19}$ hexagonal ferrites. *J. Magn. Magn Mater.*, 1984, **44**, P. 118–128.

[9] Collomb A., Obradors X., Isalgué A., Fruchart D. Neutron diffraction study of the crystallographic and magnetic structures of the $BaFe_{12-x}Mn_xO_{19}$ M-type hexagonal ferrites. *J. Magn. Magn Mater.*, 1987, **69**, P. 317–324.

[10] Thang P.D., Ho T.A., Dang N.T., Lee B.W., Phan T.L., Manh T.V., Kim D.H., Yang D.S. Mn-doped $(Ba,Y)Fe_{12}O_{19}$ hexaferrites: Crystal structure and oxidation states of Mn and Fe. *Current Applied Physics*, 2020, **20**, P. 1263–1267.

[11] Okube M., Yoshizaki J., Toyoda T., Sasaki S. Cation distribution and magnetic structure of M-type $BaTiMnFe_{10}O_{19}$ examined by synchrotron X-ray and neutron studies. *J. Appl. Cryst.*, 2016, **49**, P. 1433–1442.

[12] Adeela N., Khan U., Iqbal M., Riaz S., Ali H., Maaz K., Naseem S. Magnetic and dielectric investigations of Mn-doped Ba hexaferrite nanoparticles by hydrothermal approach. *J. Electronic Materials*, 2016, **45**, P. 5853–5859.

[13] Kim M., Lee H., Kim J. Magnetic properties of Mn substituted strontium ferrite powders synthesized by the molten salt method. *AIP Advances*, 2020, **10**, 015325.

[14] Trusov L.A., Gorbachev E.A., Lebedev V.A., Sleptsova A.E., Roslyakov I.V., Kozlyakova E.S., Vasiliev A.V., Dinnebier R.E., Jansen M., Kazin P.E. Ca–Al double-substituted strontium hexaferrites with giant coercivity. *Chem. Commun.*, 2018, **54**, P. 479–482.

[15] Petříček V., Dušek M., Palatinus L. Crystallographic Computing System JANA2006: General features. *Z. Kristallogr.-Cryst. Mater.*, 2014, **229**, P. 345–352.

[16] Shannon R.D. Revised effective ionic radii and systematic studies of interatomic distances in halides and chalcogenides. *Acta Crystallogr. A*, 1976, **32**, P. 751–767.

[17] Xu Y., Yang G.-L., Chu D.-P., Zhai H.-R. Theory of the single ion magnetocrystalline anisotropy of 3d ions. *Phys. Stat. Sol. B*, 1990, **157**, P. 685–693.

[18] Schilder H., Lueken H. Computerized magnetic studies on d, f, d–d, f–f, and d–S; f–S systems under varying ligand and magnetic fields. *J. Magn. Magn. Mater.*, 2004, **281**, P. 17–26.

[19] Tenorio-González F.N., Bolarín-Miró A.M., Sánchez-De Jesús F., Vera-Serna P., Menéndez-González N., Sánchez-Marcos J. Crystal structure and magnetic properties of high Mn-doped strontium hexaferrite. *J. Alloys Compd.*, 2017, **695**, P. 2083–2090.

*Information about the authors:*

*Pavel E. Kazin* – Department of Chemistry, Lomonosov Moscow State University, 119991 Moscow, Russia;
ORCID 0000-0002-1415-2190; kazin@inorg.chem.msu.ru

*Anastasia E. Sleptsova* – Max Planck Institute for Solid State Research, Heisenbergstrasse 1, 70569 Stuttgart, Germany;
ORCID 0000-0002-4788-2624; sleptsovaanastasia@gmail.com

*Alexander V. Vasiliev* – Department of Chemistry, Lomonosov Moscow State University, 119991 Moscow, Russia;
ORCID /0000-0003-4108-9040; a.vasiliev@inorg.chem.msu.ru

*Artem A. Eliseev* – Department of Chemistry, Lomonosov Moscow State University, 119991 Moscow, Russia;
ORCID 0000-0002-3644-9673; artem.a.eliseev@gmail.com

*Robert E. Dinnebier* – Max Planck Institute for Solid State Research, Heisenbergstrasse 1, 70569 Stuttgart, Germany;
ORCID 0000-0003-2778-2113; R.Dinnebier@fkf.mpg.de

*Sebastian Bette* – Max Planck Institute for Solid State Research, Heisenbergstrasse 1, 70569 Stuttgart, Germany;
ORCID 0000-0003-3575-0517; s.bette@fkf.mpg.de

*Conflict of interest*: the authors declare no conflict of interest.